Control of spin relaxation anisotropy by spin-orbit-coupled diffusive spin motion

Daisuke Iizasa,[1] Asuka Aoki,[1] Takahito Saito,[1] Junsaku Nitta,[1,2,3] Gian Salis,[4] and Makoto Kohda [1,2,3,5]

[1]*Department of Materials Science, Tohoku University, Sendai 980-8579, Japan*
[2]*Center for Spintronics Research Network, Tohoku University, Sendai 980-8577, Japan*
[3]*Center for Science and Innovation in Spintronics (Core Research Cluster), Tohoku University, Sendai 980-8577, Japan*
[4]*IBM Research-Zurich, Säumerstrasse 4, 8803 Rüschlikon, Switzerland*
[5]*Division for the Establishment of Frontier Sciences, Organization for Advanced Studies, Tohoku University, Sendai 980-8577, Japan*

Spatiotemporal spin dynamics under spin-orbit interaction is investigated in a (001) GaAs two-dimensional electron gas using magneto-optical Kerr rotation microscopy. Spin-polarized electrons are diffused away from the excited position, resulting in spin precession because of the diffusion-induced spin-orbit field. Near the cancellation between the spin-orbit field and the external magnetic field, the induced spin precession frequency depends nonlinearly on the diffusion velocity, which is unexpected from the conventional linear relation between the spin-orbit field and the electron velocity. This behavior originates from an enhancement of the spin relaxation anisotropy by the electron velocity perpendicular to the diffused direction. We demonstrate that the spin relaxation anisotropy, which has been regarded as a material constant, can be controlled via diffusive electron motion.

I. INTRODUCTION

Precise control of spin motion is a prerequisite from fundamental physics to spintronics and quantum information technology [1–4]. In a semiconductor quantum well (QW), Rashba [5,6] and Dresselhaus [7] spin-orbit (SO) interactions act as effective magnetic fields for moving electrons, enabling coherent spin control via precession, whereas spin relaxation occurs simultaneously because of an interplay between the SO field and the random motion of electrons [8]. Both spin precession and relaxation processes are closely tied to one another solely by SO interaction [9]. For stationary electrons with mean zero velocity, the correlation between precession and relaxation triggers a modulation of spin precessional motion, known as spin relaxation anisotropy [10–19]. For spin rotation by external and/or SO fields in a QW, spins along growth and in-plane orientations do not experience identical torques because of the in-plane orientation of the SO fields. This situation induces anisotropic spin relaxation [10–19] and modulates the spin precession frequency [13–16,18,19]. Because SO fields are well defined for stationary electrons, the spin relaxation anisotropy has been regarded as a material constant. However, for moving electrons with a finite net velocity induced by drift [20–26], diffusion [25–28], and surface acoustic wave [29], the electron trajectory further modulates SO fields and directly affects the spin relaxation anisotropy through the momentum-dependent spin precession. Moreover, the spin relaxation anisotropy is not limited to particular materials, such as III–V semiconductors because the anisotropic SO fields are ubiquitous in solid states with spin-momentum locking in topological insulators [30,31], the Rashba interface in oxides [32], metal interfaces [33], and the Zeeman-type SO field in two-dimensional materials [34]. Despite this, earlier

studies of spin relaxation anisotropy have remained limited only to stationary cases [13–16,18,19].

Here, we experimentally manifest control of spin precessional motion via spin relaxation anisotropy by diffusive spin motion in a GaAs-based QW. When the SO field under diffusive motion is nearly compensated by a constant external magnetic field, the spin precession frequency is no longer linear to the diffusion velocity. This behavior cannot be anticipated from a conventional spin drift/diffusion model. It is explained by a modulation of the spin relaxation anisotropy. The evaluated spin relaxation anisotropy, which exhibits sixfold enhancement from the stationary case, is explained by a tilting of the spin precession axis from the direction of the external magnetic field caused by the electron diffusive motion. We influence the spin relaxation anisotropy by precisely controlling the electron motion.

This paper is organized as follows. In Sec. II, we explain experimental methods, the layer structure of GaAs QW, and spin-diffusion velocity to manipulate spin precession. In Sec. III, we show the evidence of nonlinear behavior of precession frequency against spin-diffusion velocity and suggest that spin relaxation anisotropy is modulated by spin-diffusion velocity. In the subsequent Sec. IV, we theoretically elucidate and model diffusion-velocity-induced spin relaxation anisotropy. We compare our theoretical model with experimental results in Sec. V. Lastly, we close with a conclusion in Sec. VI.

II. EXPERIMENTAL METHODS

The structure examined for this paper was a modulation-doped 20-nm-thick GaAs QW grown on a semi-insulating (001) GaAs substrate by using metal-organic chemical vapor
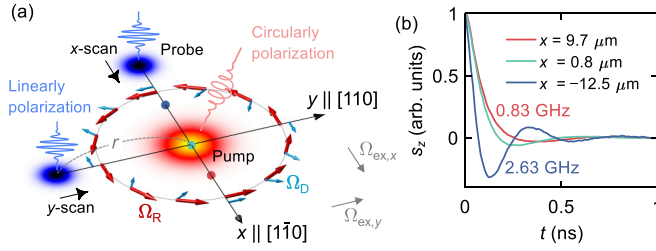
FIG. 1. (a) Sketch of a pump-probe scanning Kerr microscopy setup with Rashba ($\mathbf{\Omega}_R$), Dresselhaus ($\mathbf{\Omega}_D$), and external magnetic fields ($\mathbf{\Omega}_{ex,x}$ and $\mathbf{\Omega}_{ex,y}$) as precession vectors for y- and x-scan configurations, respectively. (b) Measured s_z at different x positions highlighted as colored circles in (a).

deposition. From the substrate side, this structure consists of a 200-nm GaAs buffer layer/[18-nm Al$_{0.3}$Ga$_{0.7}$As and 2-nm GaAs]×60 superlattice/100-nm Al$_{0.3}$Ga$_{0.7}$As/20-nm GaAs QW/30-nm Al$_{0.3}$Ga$_{0.7}$As spacer layer/20-nm Si-doped Al$_{0.3}$Ga$_{0.7}$As doping layer (6 × 10^{18} cm^{-3})/5-nm GaAs capping layer. In this system, we obtain SO fields characterized by the Rashba parameter α (<0), the Dresselhaus parameter $\beta = \beta_1 - \beta_3$ (>0) with linear $\beta_1 = -\gamma \langle k_z^2 \rangle$ and cubic term $\beta_3 = -\gamma k_F^2/4$. Here, $\langle k_z^2 \rangle$ denotes the expected value of the squared wave number in the QW. The bulk Dresselhaus coefficient is $\gamma < 0$. The Fermi wave number is $k_F = \sqrt{2\pi n_s}$. The carrier density and mobility measured using a Hall bar device were $n_s = 1.72 \times 10^{11}$ cm^{-2} and $\mu_e = 1.12 \times 10^5$ cm^2 V^{-1} s^{-1}, respectively, at 4.2 K. To detect the diffusive spin dynamics, spatiotemporal Kerr rotation microscopy is performed using a mode-locked Ti:sapphire laser emitting 2-ps-long pulses at a 79.2-MHz repetition rate. Figure 1(a) depicts an experimental configuration for pump and probe beams with Rashba and Dresselhaus SO fields. Therein, $\mathbf{\Omega}_R$ and $\mathbf{\Omega}_D$, respectively, represent the spin precession frequency vectors. A circularly polarized pump beam with Gaussian σ-width σ_{pp} is focused onto the sample surface to excite spin-polarization s_z along the growth direction. A linearly polarized probe beam (spot size σ_{pr}) detects s_z at delay time t and arbitrary position by a motor-controlled scanning mirror. All-optical measurements are taken at 30 K.

The spin precession frequency induced by an average diffusion velocity $\mathbf{v} = (v_x, v_y)$ in an external magnetic-field $\mathbf{B}_{ex} = (B_x, B_y)$ is generally described as

$$\langle \Omega_{x,y}(v_{y,x}) \rangle = \frac{2m}{\hbar^2}(\pm\alpha + \beta)v_{y,x} + \frac{g\mu_B}{\hbar}B_{x,y}. \qquad (1)$$

Here $g < 0$ stands for the electron g factor, μ_B denotes the Bohr magneton, $\hbar$ is the reduced Planck's constant, and $m = 0.067m_0$ expresses the effective electron mass of GaAs. The diffusion velocity v_{dif}, which is controlled by the center-to-center distance r between the pump and the probe spots, is defined as (see Appendix A for derivation)

$$v_{dif} = \frac{2D_s}{(2D_s\tau_s + \sigma_{eff}^2)}r, \qquad (2)$$

where D_s is the spin-diffusion constant, τ_s represents the D'yakonov-Perel' spin relaxation time, and the convoluted spot size σ_{eff} is defined by $\sigma_{eff}^2 = \sigma_{pp}^2 + \sigma_{pr}^2$ [27]. Also, τ_s is a result of the replacement of $t = \tau_s$ because our system satisfies
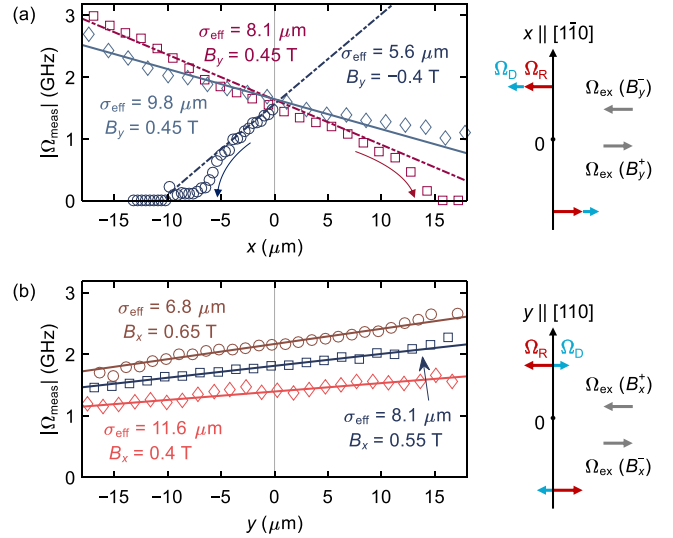

FIG. 2. Measured spin precession frequency $|\Omega_{meas}|$ obtained for different σ_{eff}'s and $\mathbf{B}_{ex}$'s and for scans of the pump-probe separation along (a) x and (b) y. All symbols represent experimental data. All solid lines show linear fits. The dashed lines in (a) correspond to the nonlinear fits based on Eq. (3) with $\Gamma_{at} = -0.076$ GHz.

$2D_s\tau_s \ll \sigma_{eff}^2$ and small τ_s. By changing the probe position along the x axis (y axis) [27], i.e., the distance r in Eq. (2), one can set the diffusion velocity $v_{dif} = v_x$ ($v_{dif} = v_y$) and thereby modulate the spin precession frequency [$\langle\Omega_y(v_x)\rangle$ or $\langle\Omega_x(v_y)\rangle$ in Eq. (1)]. Figure 1(b) shows the time evolution of the experimental Kerr signal (s_z) at different probe positions ($x = 9.7$, 0.8, and -12.5 μm) in a x-scan ($\sigma_{eff} = 8.1$ μm and $B_y = +0.45$ T). The spin precession frequency depends strongly on the probe position, reflecting the momentum- (velocity-) dependent SO field induced by the finite diffusion velocity. We systematically measured Kerr signals with different positions on the x and y axes with several spot sizes σ_{eff}. We extracted the precession frequency $|\Omega_{meas}|$ by fitting the normalized Kerr signal $s_z = \exp(-t/\tau_s)\cos(2\pi|\Omega_{meas}|t + \phi)$ with phase-shift ϕ. Besides, the spin relaxation also shows position-dependent behavior as seen in Fig. 1(b). We check this effect using numerical Monte Carlo (MC) simulation and confirm that the position-dependent spin relaxation appears. Although the origin of this modulation is an open question, it may be induced by the diffusion velocity. The model to explain the modulation of spin relaxation time in different probe positions is not well established so far.

III. EMERGENCE OF NONLINEAR VARIATION IN PRECESSION FREQUENCY

Figures 2(a) and 2(b) summarize extracted $|\Omega_{meas}|$ in x and y scans. For the y scan [Fig. 2(b)], $|\Omega_{meas}|$ varies linearly with the y position for all conditions of B_x and σ_{eff}, reflecting the linear dependence of v_{dif} on the y position as presented in Eq. (2). In addition, when σ_{eff} decreases from 11.6 to 6.8 μm, the slope $d\Omega_{meas}/dy$ increases gradually, which agrees well with Eq. (2) and which is consistent with earlier reports of the literature [20,23,24,26–28]. For the x scan [Fig. 2(a)], however, a linear variation of $|\Omega_{meas}|$ on the x position is only observed for $\sigma_{eff} = 9.8$ μm and

$B_y = +0.45$ T (diamond symbols). Reducing σ_{eff} to 8.1 and 5.6 μm exhibits a deviation from a linear variation; notably most pronounced when $|\Omega_{\text{meas}}|$ approaches zero. This cannot be explained using the conventional linear relation between electron velocity and SO field. To understand this effect, we first evaluate the SO parameters from the linear frequency variation. From linear fits depicted as solid lines in Figs. 2(a) and 2(b), we obtain $\alpha = -2.89 \times 10^{-13}$, $\beta_1 = 1.86 \times 10^{-13}$ eV m, and $\beta_3 = 0.22 \times 10^{-13}$ eV m. Also, $g = -0.268$ is estimated at $r = 0$ ($v_{\text{dif}} = 0$). We assume $g < 0$ based on the QW thickness [24]. Also, $D_s = 0.0195$ m^2/s is derived from the measured $\tau_s = 75$ ps at $\boldsymbol{B}_{\text{ex}} = \mathbf{0}$ T and $r = 0$ with large spot size $\sigma_{\text{eff}} = 30$ μm [35]. Note that the charge momentum scattering time $\tau_p = \mu_e m/e \approx 4.22$ ps is much larger than the effective momentum scattering time $\tau = 2D_s/v_F^2 \approx 1.24$ ps in our sample. Although the spin-diffusion constant is smaller than the charge-diffusion constant [36], our experiments use the spin as a label of electrons and, therefore, track the spin and not the charge diffusion. Using evaluated β_1, β_3, and n_s, we obtain $\gamma = -8.31$ eV Å^3 which is consistent with values reported in the literature [37]. To explain our observation, we introduce in analogy to anisotropic spin relaxation for stationary electrons modified spin precession frequencies [13–16,18,19],

$$\Omega_x^* = \sqrt{\langle \Omega_x(v_{\text{dif}}) \rangle^2 - \Gamma_{\text{at}}^2}, \qquad \Omega_y^* = \sqrt{\langle \Omega_y(v_{\text{dif}}) \rangle^2 - \Gamma_{\text{at}}^2},$$

$$(3)$$

where the anisotropic term [15,18] is

$$\Gamma_{\text{at}}(\Theta) = -\tfrac{1}{2}(\Gamma_x \cos^2 \Theta + \Gamma_y \sin^2 \Theta). \qquad (4)$$

Here the relaxation rate of spins oriented along the x and y axes is $\Gamma_{x,y} = (4D_s m^2/\hbar^4)[(\mp\alpha + \beta)^2 + \beta_3^2]$, respectively, and $\Theta \in [0, 2\pi]$ is the direction of the spin precession axis, defined as an in-plane polar angle from the $+x$ toward the $+y$ axis. The term $\Gamma_{\text{at}}(\Theta)$ describes the relaxation anisotropy between the two relevant orthogonal crystal axes and is responsible for a correction of the precession frequency [Eq. (3)]. For the y scan [$\boldsymbol{B}_{\text{ex}} = (B_x, 0)$], spins precess on the y-z plane and $\Gamma_{\text{at}}(\Theta = 0) = -\Gamma_x/2 = (\Gamma_y - \Gamma_z)/2$ denotes half of the difference of the relaxation rate between the y and the z axes, where $\Gamma_z = \Gamma_x + \Gamma_y$ is the relaxation rate along the z axis. For the x-scan [$\boldsymbol{B}_{\text{ex}} = (0, B_y)$], $\Gamma_{\text{at}}(\pm\pi/2) = -\Gamma_y/2$. Because $\Gamma_{\text{at}}(\Theta)$ additionally contributes to the spin precession frequency shown in Eq. (3), $\Omega_{x,y}^*$ shows a nonlinear dependence on the probe position r, which becomes pronounced when the precession frequency induced by external and SO fields becomes comparable to $\Gamma_{x,y}/2$. Based on the experimentally evaluated values for α, β_1, β_3, and D_s, we calculate $-\Gamma_y/2 = -0.076$ and $-\Gamma_x/2 = -0.99$ GHz. For $\sigma_{\text{eff}} = 5.6$ and 8.1 μm, the calculated Ω_y^*'s are shown as dashed lines in Fig. 2(a). The calculated values only reproduce the experimental data in a linear frequency region. The rapid decrease in Ω_y^* that occurs below 0.8 GHz cannot be explained by $-\Gamma_y/2 = -0.076$ GHz.

IV. VELOCITY-DEPENDENT ANISOTROPIC TERM

To obtain insights into the origin of this modulation of the anisotropic term, we first perform numerical MC simulations, which is a semiclassical calculation of spin precession based on the random walk of electron spins [38]. We use
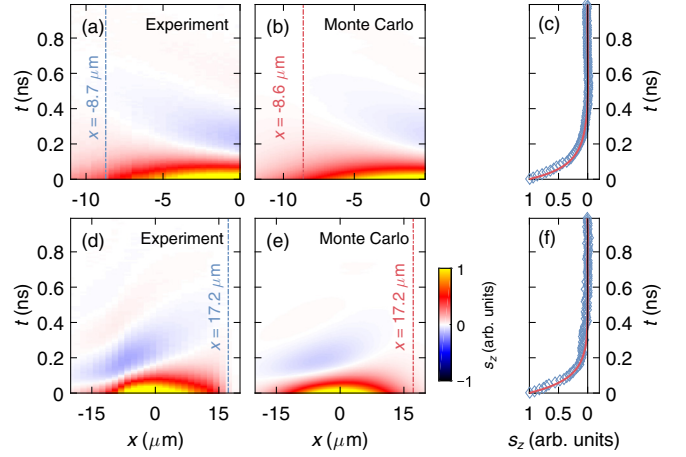

FIG. 3. Maps of Kerr signal s_z gathered along time t and spatial displacement x for experimental results (a) with $\sigma_{\text{eff}} = 5.6$ μm, $B_y = -0.4$ T and (d) with $\sigma_{\text{eff}} = 9.8$ μm, $B_y = 0.45$ T. Corresponding Monte Carlo simulations in (b) and (e) using experimentally determined SO coefficients and spot size. (c) and (f) show the line cut of s_z at around $x = -8.7$ and $x = 17.2$ μm indicated by dashed lines in the maps. The diamonds represent data from experiment, whereas solids are from Monte Carlo simulation.

the experimentally determined SO coefficients and spot sizes. Figure 3 gathers time-evolved s_z as a function of the spatial displacement for both experiment and MC simulation. For $\sigma_{\text{eff}} = 5.6$ μm and $B_y = -0.4$ T in Fig. 3(a), the spin precession halts at $x = -8.7$ μm [diamond in Fig. 3(c)]. Remarkably, the simulated s_z also shows a halt of spin precession as shown in Figs. 3(b) and 3(c). This consistency between experimental and MC simulation is also confirmed in the case of $\sigma_{\text{eff}} = 9.8$ μm and $B_y = 0.45$ T as seen in Figs. 3(d)–3(f). Importantly, in MC simulations, we probe all electron spins arrived at the probe position from pumped spins as shown in the sketch of Fig. 4(a). This indicates that the precession of all electron spins by the velocity-induced SO field and $\boldsymbol{B}_{\text{ex}}$ contributes to the spin relaxation anisotropy, and, therefore, the trajectories of diffused electrons are responsible for the unusual modulation of the anisotropic term.

More specifically, according to Eq. (4), the frequency modulation caused by the relaxation anisotropy depends on the direction of the precession axis (Θ). For stationary electrons under $\boldsymbol{B}_{\text{ex}}$, where the SO field does not contribute to frequency modulation, Θ is well defined by the direction of $\boldsymbol{B}_{\text{ex}}$. However, for moving electrons, the precession axis is defined by the sum of $\boldsymbol{B}_{\text{ex}}$ and the SO field, implying that the electron trajectories under diffusion further modulate Θ. As a result, the precession axis is no longer well defined by $\boldsymbol{B}_{\text{ex}}$ because of different diffusion velocity vectors $\boldsymbol{v} = (v_x, v_y)$ in time τ_s [different arrows in Fig. 4(a)]. Specifically examining one single trajectory with average velocity $\boldsymbol{v}$, its direction of average precession axis $\Theta(v_x, v_y) = \arctan(\langle\Omega_y(v_x)\rangle/\langle\Omega_x(v_y)\rangle)$ can be obtained from Eq. (1). Entering $\Theta(v_x, v_y)$ into Eq. (4) directly reveals the velocity-dependent form of the anisotropic term,

$$\Gamma_{\text{at}}(v_x, v_y) = -\frac{\Gamma_x \langle\Omega_x(v_y)\rangle^2 + \Gamma_y \langle\Omega_y(v_x)\rangle^2}{2(\langle\Omega_x(v_y)\rangle^2 + \langle\Omega_y(v_x)\rangle^2)}. \qquad (5)$$
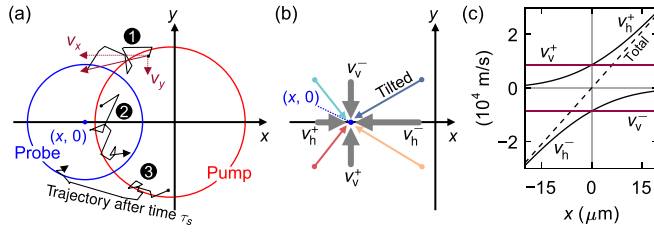
FIG. 4. (a) *x*-scan configuration where the probe center is separated by a vector $(x, 0)$ from the pump center $(0,0)$. Electron trajectories exist with an average velocity that is tilted from the *x* axis, contrary to the macroscopic diffusion velocity [Eq. (2)]. (b) Mean velocity components of horizontal and vertical directions $v_h^{\pm}$ and $v_v^{\pm}$. (c) Calculated $v_h^{\pm}$, $v_v^{\pm}$ based on Eqs. (7) and (8).

This indicates that we should account for both the *x* and the *y* components of the diffusion velocity in the trajectory. If we only consider a spatially averaged diffusion velocity that points along the *x* axis, we obtain $v_x = v_{\text{dif}}$, $v_y = 0$, and, thus, $\langle \Omega_x(v_y) \rangle = 0$. Consequently, $\Gamma_{\text{at}}(v_{\text{dif}}, 0) = -\Gamma_y/2$, and this value is too small to explain the nonlinear variation in $|\Omega_{\text{meas}}|$ as mentioned in Sec. III. This strongly suggests that the vertical velocity v_y modulates the anisotropic term. In the following, therefore, consider both the horizontal and the vertical velocity components and focus on this vertical velocity to address the experimental results.

By sorting all diffusion velocity vectors shown in Fig. 4(a) along the *x* and *y* axes according to their sign, the macroscopic diffusion velocity [Eq. (2)] can be represented by its horizontal and vertical parts [see the silver bold arrows shown in Fig. 4(b)]. That is,

$$v_{\text{dif}} = v_h^+ + v_h^- + v_v^+ + v_v^-, \qquad (6)$$

where their components are (see Appendix B for complete derivation),

$$v_h^{\pm} = \pm \sigma_{\text{eff}} \sqrt{\frac{\Sigma}{\pi \tau_s}} e^{-(r^2 \Sigma \tau_s)/\sigma_{\text{eff}}^2} + \Sigma r \, \text{erfc}\left(\mp \frac{r\sqrt{\Sigma \tau_s}}{\sigma_{\text{eff}}}\right), \quad (7)$$

$$v_v^{\pm} = \pm \sigma_{\text{eff}} \sqrt{\frac{\Sigma}{\pi \tau_s}}. \qquad (8)$$

Here $\Sigma = D_s/(2D_s\tau_s + \sigma_{\text{eff}}^2)$, and the complementary error function is denoted by erfc. The $\pm$ signs in $v_h^{\pm}$ and $v_v^{\pm}$, respectively, correspond to the positive/negative velocity components along the horizontal or vertical axes [Fig. 4(b)]. Figure 4(c) shows calculated $v_h^{\pm}$ and $v_v^{\pm}$. v_h^+ increases rapidly in the $+x$ region, whereas v_h^- has the opposite tendency because of the radial diffusion of electrons from the excited pump spot. When the probe spot is displaced along the axis [Fig. 4(a)], the average velocity vector points to the $-x$ axis because there $|v_h^-| > |v_h^+|$. Remarkably, vertical velocities $v_v^{\pm}$ are independent of probe position and are of similar size as $v_h^{\pm}$. This suggests that velocity vectors tilted away from the *x* axis modulate Γ_{at}. Therefore, the precession axis (Θ) no longer points along $\boldsymbol{B}_{\text{ex}}$. By considering the four tilted velocity vectors (v_h^+, v_v^+), (v_h^+, v_v^-), (v_h^-, v_v^+), and (v_h^-, v_v^-) at each *r* instead of the conventional macroscopic diffusion velocity vector $\boldsymbol{v} = (v_{\text{dif}}, 0)$, we obtain the anisotropic term
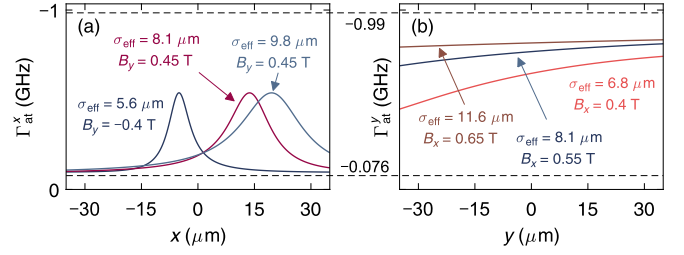

FIG. 5. (a) Calculated anisotropy term $\Gamma_{\text{at}}^{x,y}$ for the (a) *x* scan and the (b) *y* scan as obtained from using Eq. (9). Both $\Gamma_{\text{at}}^{x,y}$'s are modulated by *r*.

by averaging

$$\Gamma_{\text{at}}^x = [\Gamma_{\text{at}}(v_h^+, v_v^+) + \Gamma_{\text{at}}(v_h^+, v_v^-)$$
$$+ \Gamma_{\text{at}}(v_h^-, v_v^+) + \Gamma_{\text{at}}(v_h^-, v_v^-)]/4. \qquad (9)$$

For the *y*-scan configuration, Γ_{at}^y is obtained from Eq. (9) by flipping v_h and v_v with each other. Since Γ_x and Γ_y are constants, we can calculate the velocity-dependent anisotropic term [Eq. (9)] exactly using the subsequent Eqs. (1), (5), (7), and (8) as a function of the spatial displacement *r*. We calculate $\Gamma_{\text{at}}^{x,y}$ in Figs. 5(a) and 5(b) with parameters evaluated from the experimental conditions. The Γ_{at}^x exhibits a peak structure corresponding to the cancellation between the external and the SO fields, i.e., $\langle \Omega_y(v_{\text{dif}}) \rangle = 0$. At this position, Γ_{at}^x is enhanced by more than six times from $-\Gamma_y/2 = -0.076$ GHz. Such a peak structure is observed consistently for different spot sizes and B_y values. The enhanced Γ_{at}^x is the consequence of a tilting of the spin precession axis away from the $\boldsymbol{B}_{\text{ex}}$ direction due to the $v_v^{\pm}$ components that introduce a contribution of $\langle \Omega_x(v_v^{\pm}) \rangle^2$. As seen from Eq. (5), $\Gamma_x \langle \Omega_x(v_v^{\pm}) \rangle^2$ is introduced in the numerator of the expression for Γ_{at}. For the *y* scan, Γ_{at}^y is only gently modulated with *y* because, in this case, the additional contribution proportional to $\Gamma_y \langle \Omega_y(v_v^{\pm}) \rangle$ is weak compared to the case of the *x* scan (because $\Gamma_x \gg \Gamma_y$). In other words, a small SO field along the *y* axis does not tilt the spin precession axis significantly. In both *x* and *y* scans when the magnitude of $\boldsymbol{B}_{\text{ex}}$ becomes sufficiently large compared to the SO field, $\Gamma_{\text{at}}^{x,y}$ converges, respectively, to the stationary cases of -0.076 and -0.99 GHz.

V. COMPARISON WITH EXPERIMENT

Finally, we compare our model with experimental results to address the nonlinear behavior of *x* scans by using $\Gamma_{\text{at}}^{x,y}$ in Fig. 5. Figures 6(a) and 6(b) show frequency analysis for $\sigma_{\text{eff}} = 5.6\ \mu$m with $B_y = -0.4$ T and $\sigma_{\text{eff}} = 8.1\ \mu$m with $B_y = 0.45$ T, respectively. The solid and dashed lines, respectively, correspond to the calculated Ω_y^* based on Eq. (3) with our new Γ_{at}^x [Eq. (9)] and the conventional $-\Gamma_y/2 = -0.076$ GHz. The remaining parameters of Eq. (3) are all experimentally obtained. The Ω_y^* obtained with the new Γ_{at}^x shows excellent agreement with the experimental values, including the nonlinear variation. We also compare the *y* scan by MC simulation for parameters $\sigma_{\text{eff}} = 5.6\ \mu$m and $B_x = 0.4$ T [Fig. 6(c)]. The solid and dashed lines are calculated values of Ω_x^* with new Γ_{at}^y and conventional $-\Gamma_x/2 = -0.99$ GHz, respectively, where Ω_x^* is enhanced for negative *y* values for new Γ_{at}^y. This point is confirmed further in Fig. 6(d) by plotting the
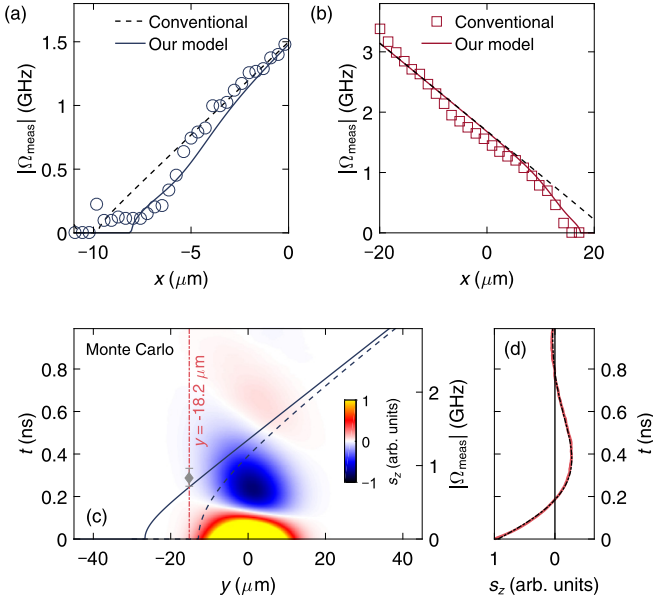
FIG. 6. The frequency analysis is shown for x scans for (a) $\sigma_{\text{eff}} = 5.6 \ \mu$m at $B_y = -0.4$ T and for (b) $\sigma_{\text{eff}} = 8.1 \ \mu$m at $B_y = 0.45$ T. All solid lines are Ω_y^* calculated with new Γ_{at}^x, and dashed lines are with the conventional anisotropic term $-\Gamma_y/2 = -0.076$ GHz. (c) MC simulated time-space records of s_z in a y scan with $\sigma_{\text{eff}} = 5.6 \ \mu$m, $B_x = 0.4$ T, and $g = -0.268$: the solid line shows Ω_x^* with new Γ_{at}^y; the dashed line is obtained with the conventional value of $-\Gamma_x/2 = -0.99$ GHz. The gray diamond is the extracted frequency from the (d) time evolution of s_z at $y = -18.2 \ \mu$m with the MC simulation (red solid) and the fitted curve (dotted black).

time evolution of s_z at $y = -18.2 \ \mu$m. The spin precession frequency obtained from the MC simulation at $y = -18.2 \ \mu$m [gray diamond in Fig. 6(c)] shows good agreement with our new model.

Throughout this paper, we assume a constant D_s since we observe a linear variation of $|\Omega_{\text{meas}}|$ for x and y scans. Moreover, Monte Carlo simulations with constant D_s well reproduce our experimental results, showing the evidence against the possibility of a variation of D_s with spatial separation r [39]. The quantitative agreement shown above reveals clearly that precession by the relaxation anisotropy is not a material constant parameter but is rather controlled by diffusive spin motion.

VI. CONCLUSION

In conclusion, we measured the precession frequency in an external magnetic field by changing the relative distance between the excited pump and the detected probe positions in a spatiotemporal Kerr rotation microscope. Because of various electron trajectories for electrons traveling from the pump to the probe position, the spin precession axis is tilted substantially from the external magnetic-field direction when the diffusion-induced SO field nearly compensates the magnitude of the external magnetic field. It is detected as a nonlinear precession frequency modulation. Whereas the relaxation anisotropy is regarded as a constant parameter for stationary electrons, it becomes controllable for moving electrons. Because this effect is not only limited only to diffusive motion,

but also can be controlled by drift and ballistic transport, our findings link the effect of the precise control of spin states to future spintronics and quantum information technology.

APPENDIX A: AVERAGE SPIN-DIFFUSION VELOCITY

Let us consider a simple case for the diffusion of the single electron spin which is arrived at position r from somewhere x after time t. The diffusion velocity of the electron spin is approximated by using the start and end positions,

$$v_{\text{dif}}^{\text{single}} = \frac{r - x}{t}. \tag{A1}$$

On the other hand, probability $\mathcal{P}$ for which an electron arrives at r from x is governed by

$$\mathcal{P} = \frac{1}{2\sqrt{\pi D_s t}} \exp\left[-\frac{(x-r)^2}{4 D_s t}\right] \tag{A2}$$

using spin-diffusion constant D_s. Note that $\mathcal{P}$ is normalized to unity. One needs to consider all trajectories that pumped electron spins arrive at the probe position. This equals to take the average diffusion velocity over convoluted laser distribution $N_{\text{eff}} = \exp[-x^2/(2\sigma_{\text{eff}}^2)]$. This corresponds to

$$v_{\text{dif}} = \frac{\int_{-\infty}^{\infty} \mathcal{P} N_{\text{eff}} v_{\text{dif}}^{\text{single}} \, dx}{\int_{-\infty}^{\infty} \mathcal{P} N_{\text{eff}} \, dx} \tag{A3}$$

$$= \frac{2 D_s}{2 D_s t + \sigma_{\text{eff}}^2} r. \tag{A4}$$

As a result, average spin-diffusion velocity can be controlled by the center-to-center distance r with linear relation. Although electron spins arrived at r from far away have infinite velocity, these large velocities are weighted by low probability at the same time. For the limit of $2 D_s t \ll \sigma_{\text{eff}}^2$ as mentioned in the main text, we can replace t with D'yakonov-Perel' spin relaxation time τ_s as far as τ_s is short.

APPENDIX B: DECOMPOSITION OF SPIN-DIFFUSION VELOCITY INTO HORIZONTAL AND VERTICAL DIFFUSION VELOCITIES

By changing the order of the integral in Eq. (A3), we can sort diffusion velocity with its sign,

$$v_{\text{dif}} = \frac{\int_{-\infty}^{r} \mathcal{P} N_{\text{eff}} v_{\text{dif}}^{\text{single}} \, dx}{\int_{-\infty}^{\infty} \mathcal{P} N_{\text{eff}} \, dx} + \frac{\int_{r}^{\infty} \mathcal{P} N_{\text{eff}} v_{\text{dif}}^{\text{single}} \, dx}{\int_{-\infty}^{\infty} \mathcal{P} N_{\text{eff}} \, dx}. \tag{B1}$$

The first term on the right-hand side of Eq. (B1) samples diffusion velocity from the position x ($< r$) to ($r, 0$), representing positive diffusion velocity v_{h}^{+} [cf. Eq. (A1)], whereas the second term samples negative diffusion velocity v_{h}^{-}. From Eq. (7) in the main text, we also find diffusion velocity exists even at $r = 0$, and this is indeed always existing vertical velocity $v_{\mathrm{v}}^{\pm}$.

[1] S. A. Wolf, D. D. Awschalom, R. A. Buhrman, J. M. Daughton, S. von Molnár, M. L. Roukes, A. Y. Chtchelkanova, and D. M. Treger, Science **294**, 1488 (2001).

[2] D. D. Awschalom and M. E. Flatté, Nat. Phys. **3**, 153 (2007).

[3] B. Behin-Aein, D. Datta, S. Salahuddin, and S. Datta, Nat. Nanotechnol. **5**, 266 (2010).

[4] M. M. Waldrop, Nature (London) **530**, 144 (2016).

[5] E. I. Rashba, Fiz. Tverd. Tela **2**, 1224 (1960) [Sov. Phys. Solid State **2**, 1109 (1960)].

[6] Y. A. Bychkov and E. I. Rashba, J. Phys. C Solid State Phys. **17**, 6039 (1984).

[7] G. Dresselhaus, Phys. Rev. **100**, 580 (1955).

[8] M. I. D'yakonov and V. I. Perel', Fiz. Tverd. Tela **13**, 3581 (1971) [Sov. Phys. Solid State **13**, 3023 (1972)].

[9] J. Nitta, T. Akazaki, H. Takayanagi, and T. Enoki, Phys. Rev. Lett. **78**, 1335 (1997).

[10] N. S. Averkiev and L. E. Golub, Phys. Rev. B **60**, 15582 (1999).

[11] N. S. Averkiev, L. E. Golub, and M. Willander, J. Phys. Condens. Matter **14**, R271 (2002).

[12] J. Kainz, U. Rössler, and R. Winkler, Phys. Rev. B **68**, 075322 (2003).

[13] S. Döhrmann, D. Hägele, J. Rudolph, M. Bichler, D. Schuh, and M. Oestreich, Phys. Rev. Lett. **93**, 147405 (2004).

[14] K. Morita, H. Sanada, S. Matsuzaka, C. Y. Hu, Y. Ohno, and H. Ohno, Appl. Phys. Lett. **87**, 171905 (2005).

[15] N. S. Averkiev, L. E. Golub, A. S. Gurevich, V. P. Evtikhiev, V. P. Kochereshko, A. V. Platonov, A. S. Shkolnik, and Y. P. Efimov, Phys. Rev. B **74**, 033305 (2006).

[16] L. Schreiber, D. Duda, B. Beschoten, G. Güntherodt, H.-P. Schönherr, and J. Herfort, Phys. Rev. B **75**, 193304 (2007).

[17] D. Stich, J. H. Jiang, T. Korn, R. Schulz, D. Schuh, W. Wegscheider, M. W. Wu, and C. Schüller, Phys. Rev. B **76**, 073309 (2007).

[18] A. V. Larionov and L. E. Golub, Phys. Rev. B **78**, 033302 (2008).

[19] M. Griesbeck, M. M. Glazov, E. Y. Sherman, D. Schuh, W. Wegscheider, C. Schüller, and T. Korn, Phys. Rev. B **85**, 085313 (2012).

[20] Y. Kato, R. C. Myers, A. C. Gossard, and D. D. Awschalom, Nature (London) **427**, 50 (2004).

[21] S. A. Crooker and D. L. Smith, Phys. Rev. Lett. **94**, 236601 (2005).

[22] L. Meier, G. Salis, I. Shorubalko, E. Gini, S. Schön, and K. Ensslin, Nat. Phys. **3**, 650 (2007).

[23] M. Studer, M. P. Walser, S. Baer, H. Rusterholz, S. Schön, D. Schuh, W. Wegscheider, K. Ensslin, and G. Salis, Phys. Rev. B **82**, 235320 (2010).

[24] M. P. Walser, U. Siegenthaler, V. Lechner, D. Schuh, S. D. Ganichev, W. Wegscheider, and G. Salis, Phys. Rev. B **86**, 195309 (2012).

[25] P. Altmann, F. G. G. Hernandez, G. J. Ferreira, M. Kohda, C. Reichl, W. Wegscheider, and G. Salis, Phys. Rev. Lett. **116**, 196802 (2016).

[26] T. Saito, A. Aoki, J. Nitta, and M. Kohda, Appl. Phys. Lett. **115**, 052402 (2019).

[27] M. Kohda, P. Altmann, D. Schuh, S. D. Ganichev, W. Wegscheider, and G. Salis, Appl. Phys. Lett. **107**, 172402 (2015).

[28] K. Kawaguchi, T. Fukasawa, I. Takazawa, H. Shida, Y. Saito, D. Iizasa, T. Saito, T. Kitada, Y. Ishitani, M. Kohda, and K. Morita, Appl. Phys. Lett. **115**, 172406 (2019).

[29] O. D. D. Couto, F. Iikawa, J. Rudolph, R. Hey, and P. V. Santos, Phys. Rev. Lett. **98**, 036603 (2007).

[30] D. Hsieh, Y. Xia, L. Wray, D. Qian, A. Pal, J. H. Dil, J. Osterwalder, F. Meier, G. Bihlmayer, C. L. Kane, Y. S. Hor, R. J. Cava, and M. Z. Hasan, Science **323**, 919 (2009).

[31] M. Z. Hasan and C. L. Kane, Rev. Mod. Phys. **82**, 3045 (2010).

[32] A. D. Caviglia, M. Gabay, S. Gariglio, N. Reyren, C. Cancellieri, and J.-M. Triscone, Phys. Rev. Lett. **104**, 126803 (2010).

[33] F. Meier, H. Dil, J. Lobo-Checa, L. Patthey, and J. Osterwalder, Phys. Rev. B **77**, 165431 (2008).

[34] H. Yuan, M. S. Bahramy, K. Morimoto, S. Wu, K. Nomura, B.-J. Yang, H. Shimotani, R. Suzuki, M. Toh, C. Kloc, X. Xu, R. Arita, N. Nagaosa, and Y. Iwasa, Nat. Phys. **9**, 563 (2013).

[35] T. Henn, L. Czornomaz, and G. Salis, Appl. Phys. Lett. **109**, 152104 (2016).

[36] H. Zhao, M. Mower, and G. Vignale, Phys. Rev. B **79**, 115321 (2009).

[37] M. Kohda and G. Salis, Semicond. Sci. Technol. **32**, 073002 (2017).

[38] A. A. Kiselev and K. W. Kim, Phys. Rev. B **61**, 13115 (2000).

[39] T. Henn, T. Kiessling, W. Ossau, L. W. Molenkamp, D. Reuter, and A. D. Wieck, Phys. Rev. B **88**, 195202 (2013).